# Three-dimensional periodic complex structures in soft matter: investigation using scattering methods

## Marianne Impéror-Clerc*

*Laboratoire de Physique des Solides, Université Paris-Sud, Bat 510, Orsay, France*

Three-dimensional periodic complex structures are encountered in various soft matter systems such as liquid crystals, block-copolymer phases and the related nano-structured materials. Here, we review several well-defined topologies: two-dimensional hexagonal phase, three-dimensional packing of spheres, tetrahedral close packing (*tcp*) bi-continuous and tri-continuous cubic phases. We illustrate how small-angle X-ray scattering experiments help us to investigate these different structures and introduce the main available structural models based on both direct and inverse methods.

**Keywords: hexagonal phases; cubic phases; *tcp* phases; nano-structured materials; small-angle X-ray scattering; X-ray scattering**

## 1. INTRODUCTION

Three-dimensional periodic complex fluids with different architectures can form based on the nano-segregation between two incompatible components at the molecular level. Since the 1970s, many soft matter systems have shown this phenomenon in liquid-crystalline (LC) phases, including thermotropic molecules, surfactants, block-copolymers and lipids. Nowadays, thanks to the development over the last 15 years of the synthesis of nano-structured materials using surfactants as structure-directing agents, the same architectures are encountered in hybrid materials and porous materials. In this area, many application fields are in development such as porous media in catalysis, nano-molds to synthesize nano-particles of controlled size or biomaterials for drug delivery or bone tissue regeneration. These structures have therefore generated considerable interest in the soft matter and the materials fields.

Small-angle scattering (SAS) is a widespread technique to investigate these structures and it has been essential to elucidate new phases. In contrast with atomic or molecular crystals, the basic units are supra-molecular aggregates of a few nanometres. We first introduce here the basic methods and specificities with SAS dealing with mesophases and nano-structured materials. After that we give an overview of the available structural models, with a special emphasis on the use of intensity measurements. The different phases discussed in this paper are given in table 1: two-dimensional hexagonal phase, three-dimensional packing of spheres, tetrahedral close packing (*tcp*), bi-continuous

and tri-continuous cubic phases. This list corresponds to all the three-dimensional phases found experimentally for which the driving force is the segregation between two incompatible molecular blocks. The case of the lamellar/smectic phase is not included here because stacking of layers corresponds to a quasi-one dimensional long-range order, and this implies a different structural approach. In the same way, mesophases based on orientational order (nematic phases, blue phases ... ) or a combination of orientational and positional order (smectic blue phases, smectic Q phases ... ) are out of the scope of this paper, as we focus here on the case of structures exhibiting only long-range positional order.

## 2. MEASUREMENTS WITH SMALL-ANGLE SCATTERING

SAS is a well-known method to investigate structural properties in many soft matter systems, using either X-rays (SAXS) or neutrons (SANS) at length scales ranging from 1 to 100 nm. Dealing with periodic structures, the main feature in SAS is the presence of several Bragg peaks, because of long-range order organization at the nano-scale, as illustrated in figure 1. These Bragg peaks do not come from the crystalline arrangements of atoms as in usual crystallography, but reveal a periodicity inside matter at a molecular level between supra-molecular entities. Usually, only a very small number (typically 10 of them or less) of Bragg reflections are recorded. From their positions in reciprocal space, one can deduce the unit cell dimensions, its symmetry elements and the space group. For each phase, the list of the observed reflections is given in table 1. The space-group identification step is quite straightforward, but, when only a small number of Bragg peaks are observed, the choice of space-group is often based on additional hypothesis and when different space-groups are possible, the space-group with the highest

*\*marianne.imperor@u-psud.fr*

Table 1. List of the different three-dimensional phases discussed in this paper. For each of them, the space-group and the sequence of the Bragg reflections are provided [1]. For each Bragg reflection, the Miller indices are given with the value of $s^2$ and the multiplicity $m$ inside brackets. Depending on the symmetry of the phase, notations are as follows: three-dimensional cubic: $hkl$ ($s^2 = h^2 + k^2 + l^2$, $m$); three-dimensional hexagonal: $hkl$ ($s^2 = (4/3)(h^2 + k^2 + hk) + (1/R^2)l^2$, $m$) with $R = c/a \approx (8/3)^{1/2}$; two-dimensional hexagonal: $hk$ ($s^2 = h^2 + k^2 + hk$, $m$); three-dimensional tetragonal: $hkl$ ($s^2 = h^2 + k^2 + (1/R^2)l^2$, $m$) with $R = c/a$. Miller indices are written in bold script when they correspond to a usually strong Bragg reflection.

| type | space-group | Bragg reflections | references |
|---|---|---|---|
| three-dimensional micellar sphere packing | I$m\bar{3}m$ (*bcc*) | **110** (2, 12), *200* (4, 6), *211* (6, 24), *220* (8, 12), *310* (10, 24), *222* (12, 8), *321* (14, 48), *400* (16, 6) ... | |
| | F$m\bar{3}m$ (*fcc*) | **111** (3, 8), *200* (4, 6), *220* (8, 12), *311* (11, 24), *222* (12, 8), *400* (16, 6), *331* (19, 24), *420* (20, 24), *422* (24, 24), *511* (27, 24)), *333* (27, 8), *440* (32, 12), ... | |
| | P$6_3/mmc$ (*hcp*) | *100* (4/3, 6), *002* (4/$R^2$, 2), *101* (4/3+1/$R^2$, 12), *102* (4/3+4/$R^2$, 12), *110* (4, 6), *103* (4/3+9/$R^2$, 12), *200* (16/3, 6), *112* (4+4/$R^2$, 12), *201* (16/3+1/$R^2$, 12) ... | [2] |
| three-dimensional micellar (*tcp*) tetrahedral close packing | P$m\bar{3}n$ | *110* (2, 12), **200** (4, 6), **210** (5, 24), **211** (6, 24), *220* (8, 12), *310* (10, 24), *222* (12, 8), *320* (13, 24), *321* (14, 48), *400* (16, 6) ... | [3] |
| | F$d\bar{3}m$ | *111* (3, 8), **220** (8, 12), **311** (11, 24), *222* (12, 8), **400** (16, 6), *331* (19, 24), *422* (24, 24), *511* (27, 24), *333* (27, 8), *440* (32, 12) ... | [4] |
| | P$4_2/mnm$ | **311** (10+1/$R^2$, 16), *002* (4/$R^2$, 2), *112* (2+4/$R^2$, 8), **410** (17, 8), **330** (18, 4), **202** (4+4/$R^2$, 8), **212** (5+4/$R^2$, 16), **411** (17+1/$R^2$, 16), **331** (18+1/$R^2$, 8), **222** (8+4/$R^2$, 8), **312** (10+4/$R^2$, 16) ... | [5,6] |
| two-dimensional hexagonal | P$6/mm$ | **10** (1, 6), *11* (3, 6), *20* (4, 6), *21* (7, 12), *30* (9, 6), *22* (12, 6), *31* (13, 12) ... | |
| bi-continuous cubic | I$a\bar{3}d$ (G-surface) | **211** (6, 24), **220** (8, 12), *321* (14, 48), *400* (16, 6), *420* (20, 24), *332* (22, 24), *422* (24, 24), *431* (26, 48), *521* (30, 48), *440* (32, 12) ... | [7] |
| | P$n\bar{3}m$ (D-surface) | **110** (2, 12), **111** (3, 8), *200* (4, 6), *211* (6, 24), *220* (8, 12), *221* (9, 24), *310* (10, 24), *311* (11, 24) ... | |
| | I$m\bar{3}m$ (P-surface) | **110** (2, 12), *200* (4, 6), **211** (6, 24), *220* (8, 12), *310* (10, 24), *222* (12, 8), *321* (14, 48), *400* (16, 6), ... | |
| tri-continuous cubic | I$m\bar{3}m$ | *110* (2, 12), *200* (4, 6), *211* (6, 24), *220* (8, 12), *310* (10, 24), *222* (12, 8), **321** (14, 48), **400** (16, 6), *411* (18, 24), *330* (18, 12), *420* (20, 24), *332* (22, 24), *422* (24, 24) ... | [8] |

symmetry is chosen. For example, for cubic phases, one always assumes that the point group is $m\bar{3}m$, and this corresponds to the presence of an inversion centre and mirrors perpendicular to the fourfold and twofold axis. However, the knowledge of the space-group is not sufficient for structure identification. For example, in table 1, three different phases have the same space-group I$m\bar{3}m$: the *bcc* phase, the P-surface bi-continuous cubic phase and the tri-continuous cubic phase. In order to distinguish between these three structures, one has to take into account not only the positions but also the intensities of the Bragg peaks. Therefore, this paper focuses on the elaboration of structural models based on these intensities. Indeed, because the dimensions of the basic structural units (the supra-molecular entities) are comparable to the size of the unit cell, their molecular form factor gives rise to strong modulations of the Bragg peak intensities. First, we discuss how to take Bragg peak intensity measurements with SAS experiments. We detail how the usual expressions of the scattered intensity from standard crystallography using discrete atomic coordinates are modified in the case of SAS. In that case, we are able to derive the expressions of the scattered intensity in absolute scale, including all the pre-factors. As SAXS is much more

suitable than SANS to measure Bragg peaks with a good resolution, we will give the intensity expressions only in the case of X-rays.

We start from the general expression of the scattered intensity for SAXS in absolute scale[1] defined as

$$I(\boldsymbol{q}) = \frac{r_e^2}{V_{tot}} \langle |A(\boldsymbol{q})|^2 \rangle$$

with $$A(\boldsymbol{q}) = \int_{V_{tot}} \rho(\boldsymbol{r}) e^{-i\boldsymbol{q}\cdot\boldsymbol{r}} d\boldsymbol{r}.$$

(2.1)

where $r_e = 2.81794 \times 10^{-15}$ m is the classical radius of the electron, $V_{tot}$ is the sample volume illuminated by the X-ray beam and $\boldsymbol{q}$ is the scattering vector in the reciprocal-space. The modulus of the scattering vector is $q = 4\pi \sin(\theta)/\lambda$, where $2\theta$ is the scattering angle and $\lambda$ is the wavelength of X-rays. In an SAXS

[1]The intensity $I(\boldsymbol{q})$ in absolute scale is in units of the inverse of a length $[L^{-1}]$ usually expressed in cm$^{-1}$ or mm$^{-1}$. Experimentally, intensity measurements in absolute scale are made using a calibration sample. For SAXS, one can use the constant intensity contribution of water equal to 0.016 cm$^{-1}$. For SANS, the constant incoherent scattering signal from a 1 mm thick water ($H_2O$) sample is a widespread standard. In addition, corrections by the transmission of the sample and by the background contribution have to be done using standard procedures.
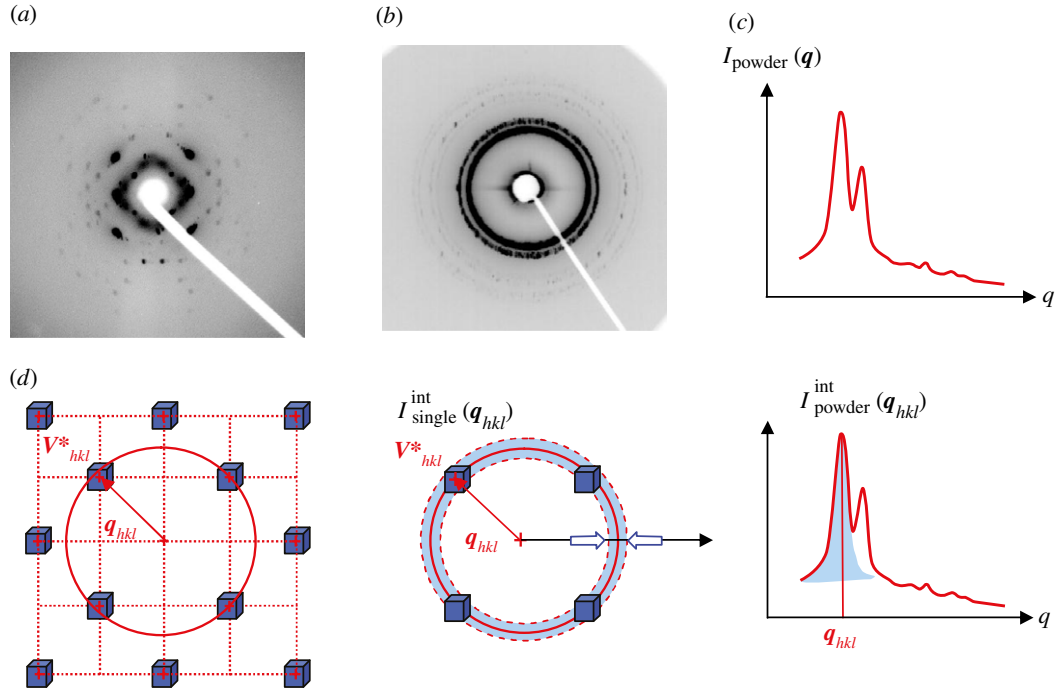
Figure 1. Typical SAXS pattern of a bi-continuous $Ia\bar{3}d$ phase [9]: (a) single-crystal pattern along a fourfold axis, (b) powder pattern and (c) the radially averaged powder intensity. (d) Relationships in reciprocal space between the integrated intensity of an individual Bragg peak $I_{\text{single}}^{\text{int}}(\boldsymbol{q}_{hkl})$ and the integrated powder intensity $I_{\text{powder}}^{\text{int}}(\boldsymbol{q}_{hkl})$. The radially averaged intensity for a powder sample $I_{\text{powder}}(q)$ takes into account the multiplicity $m_{hkl}$ of the $hkl$ reflection and the isotropic average over the orientation in space.

measurement, the fundamental quantity derived is the Fourier transform $A(\boldsymbol{q})$ of the electron density $\rho(\boldsymbol{r})$, the number of electrons per unit volume. Using the electron density, matter is described at the nano-scale as a continuous medium, and the scattered intensity reflects the spatial repartition of high- and low-electron density regions. Note that one can either define for SAXS a scattering length density (SLD) $\rho_{\text{SLD}}(\boldsymbol{r}) = r_e\rho(\boldsymbol{r})$, similar to the coherent SLD in neutron scattering (SANS), which is associated with the nuclei of the atoms. In the general case, an ensemble average (brackets notation $\langle |A(\boldsymbol{q})|^2 \rangle$) over different configurations of the system upon time and disorder factors has to be taken into account.

Only relative variations of the electron density $\rho(\boldsymbol{r})$ with respect to a constant electron density level contribute to the measured intensity. This can be shown writing $\rho(\boldsymbol{r}) = \rho_0 + \Delta\rho(\boldsymbol{r})$, where $\rho_0$ is a constant, such as the solvent electron density for a colloidal or micellar solution, or the average electron density for a periodic structure.

$$A(\boldsymbol{q}) = \int_{V_{\text{tot}}} \rho(\boldsymbol{r})e^{-i\boldsymbol{q}\cdot\boldsymbol{r}}d\boldsymbol{r}$$

$$= \int_{V_{\text{tot}}} \Delta\rho(\boldsymbol{r})e^{-i\boldsymbol{q}\cdot\boldsymbol{r}}d\boldsymbol{r} + \rho_0\int_{V_{\text{tot}}} e^{-i\boldsymbol{q}\cdot\boldsymbol{r}}d\boldsymbol{r}$$

$$\cong \int_{V_{\text{tot}}} \Delta\rho(\boldsymbol{r})e^{-i\boldsymbol{q}\cdot\boldsymbol{r}}d\boldsymbol{r}. \qquad (2.2)$$

Because the total sample volume $V_{\text{tot}}$ is always assumed to be macroscopic, the second integral over $V_{\text{tot}}$ can be neglected in $A(\vec{q})$, as it contributes only for very small scattering vector moduli that are not accessible experimentally.

For SAS, the scattering angles are small (less than typically $5°$) and $\cos\theta \cong 1$. As in standard crystallography, intensity is recorded in reciprocal space only for scattering vectors $\boldsymbol{q}$ located on the Ewald sphere. The intersection with the Ewald sphere gives rise to a geometrical correction (Lorentz factor) in the measured intensities that depends on the scattering angle. However, because $\cos\theta \cong 1$, the Lorentz factor can be neglected in the intensity expressions. Similarly, the polarization factor is equal to one for SAS.

For a three-dimensional periodic structure, the electron density $\rho(\boldsymbol{r})$ is a three-dimensional periodic function, and the amplitude can be factorized as follows:

$$A(\boldsymbol{q}) = \left(\int_{V_C} \rho(\boldsymbol{r})e^{-i\boldsymbol{q}\cdot\boldsymbol{r}}d\boldsymbol{r}\right)\sum_{i=1}^{N} e^{-i\boldsymbol{q}\cdot\boldsymbol{R}_i}$$

$$= F(\boldsymbol{q})\sum_{i=1}^{N} e^{-i\boldsymbol{q}\cdot\boldsymbol{R}_i}$$

$$= F(\boldsymbol{q})\left(\sum_{m=1}^{N_a-1} e^{-im\boldsymbol{q}\cdot\boldsymbol{a}}\right)\left(\sum_{n=1}^{N_b-1} e^{-in\boldsymbol{q}\cdot\boldsymbol{b}}\right)$$

$$\times \left(\sum_{p=1}^{N_c-1} e^{-ip\boldsymbol{q}\cdot\boldsymbol{c}}\right), \qquad (2.3)$$

with

$$F(\boldsymbol{q}) = \int_{V_C} \rho(\boldsymbol{r})e^{-i\boldsymbol{q}\cdot\boldsymbol{r}}d\boldsymbol{r}, \qquad (2.4)$$

where $V_C$ is the volume of the unit cell defined by the basis vectors $(\boldsymbol{a},\boldsymbol{b},\boldsymbol{c})$, $N = N_aN_bN_c$ is the total number of unit cells and $\{\boldsymbol{R}_i\}$ are the lattice vectors $\boldsymbol{R}_i = m\boldsymbol{a} +$

$n\boldsymbol{b} + p\boldsymbol{c}$. Like in crystallography, we can introduce the Laue function

$$\mathsf{L}(x, N) = \left(\frac{\sin(Nx)}{\sin(x)}\right)^2 \quad \text{in} \quad A(\boldsymbol{q}):$$

$$|A(\boldsymbol{q})|^2 = |F(\boldsymbol{q})|^2 \mathsf{L}\left(\frac{\boldsymbol{q} \cdot \boldsymbol{a}}{2}, N_a\right) \mathsf{L}\left(\frac{\boldsymbol{q} \cdot \boldsymbol{b}}{2}, N_b\right) \mathsf{L}\left(\frac{\boldsymbol{q} \cdot \boldsymbol{c}}{2}, N_c\right).$$
$$(2.5)$$

For a perfectly ordered structure, all unit cells are identical and the electron density corresponds to the average structure inside the unit cell ($|F(\boldsymbol{q})|^2 = \langle |F(\boldsymbol{q})|^2 \rangle$). The intensity can be written as

$$I(\boldsymbol{q}) = \frac{r_{\mathrm{e}}^2}{V_{\mathrm{tot}}} |F(\boldsymbol{q})|^2 \sum_{i=1}^N \sum_{j=1}^N \mathrm{e}^{-\mathrm{i}\boldsymbol{q}\cdot(\boldsymbol{R}_i - \boldsymbol{R}_j)}$$

$$= \frac{r_e^2}{V_{\mathrm{tot}}} N |F(\boldsymbol{q})|^2 S(\boldsymbol{q}), \qquad (2.6)$$

where $S(\boldsymbol{q})$ is the structure factor associated with the three-dimensional lattice:

$$S(\boldsymbol{q}) = \frac{1}{N} \sum_{i=1}^N \sum_{j=1}^N \mathrm{e}^{-\mathrm{i}\boldsymbol{q}\cdot(\boldsymbol{R}_i - \boldsymbol{R}_j)}$$

$$= \frac{1}{N} \mathsf{L}\left(\frac{\boldsymbol{q} \cdot \boldsymbol{a}}{2}, N_a\right) \mathsf{L}\left(\frac{\boldsymbol{q} \cdot \boldsymbol{b}}{2}, N_b\right) \mathsf{L}\left(\frac{\boldsymbol{q} \cdot \boldsymbol{c}}{2}, N_c\right).$$
$$(2.7)$$

For a large number of unit cells (macroscopic crystal), the three integers $N_a$, $N_b$ and $N_c$ are large, and the intensity is concentrated inside Bragg peaks located at the nodes of the reciprocal lattice: $\vec{q}_{hkl} = 2\pi(h\vec{a}^* + k\vec{b}^* + l\vec{c}^*)$. It is only in the ideal case of an infinite crystal that the Bragg peaks reduce to points in the reciprocal space. For a crystal of finite size, the Bragg peaks are extended to a small volume in the reciprocal space that is linked to the shape of the crystal as described by the Laue functions [10]. However, with a standard resolution of an SAS experiment, this effect may be detectable only for very small crystals (typically less than $0.1$–$0.3\,\mu\mathrm{m}$). The most usual situation is that the crystals are large enough so that the measured extension of the Bragg peaks is fixed by the experimental resolution and not by the size of the crystals. Then, the relevant quantity to introduce is the integrated intensity of a Bragg peak in reciprocal space. Its expression can be obtained by integrating the expression with the Laue functions for each Bragg peak within a small reciprocal volume $V_{hkl}^*$ around it. For a single crystal, this integrated intensity $I_{\mathrm{single}}^{\mathrm{int}}(\boldsymbol{q}_{hkl})$ is well approximated by

$$I_{\mathrm{single}}^{\mathrm{int}}(\boldsymbol{q}_{hkl}) = \frac{r_{\mathrm{e}}^2}{V_{\mathrm{tot}}} \int_{V_{hkl}^*} |A(\boldsymbol{q}_{hkl} + \boldsymbol{q})|^2 \mathrm{d}\boldsymbol{q}$$

$$\cong \frac{N}{V_{\mathrm{tot}}} r_{\mathrm{e}}^2 |F_{hkl}|^2 \frac{(2\pi)^3}{V_{\mathrm{c}}} \qquad (2.8)$$

with

$$F_{hkl} = \int_{V_{\mathrm{C}}} \rho(\boldsymbol{r}) \mathrm{e}^{-\mathrm{i}\boldsymbol{q}_{hkl}\cdot\boldsymbol{r}} \mathrm{d}\boldsymbol{r}. \qquad (2.9)$$

For a fixed position of a single crystal, the intersection with the Ewald sphere gives rise to asymmetric patterns on a two-dimensional detector. This is because, even if the scattering angles are small, Bragg peaks at $\boldsymbol{q}_{hkl}$ and $-\boldsymbol{q}_{hkl}$ are not simultaneously in reflection position on the Ewald sphere. Then, for a single crystal, one needs to rotate the sample in order to collect the integrated intensity of the Bragg peaks. For example, in figure 1a, the two-dimensional scattering pattern was recorded when applying to the sample oscillations of a few degrees in amplitude around the vertical axis, to allow the different Bragg peaks to cross the Ewald sphere. The rotation of the sample has then to be taken into account for intensity measurements.[2]

Reliable measurements of the integrated intensity are easier to obtain with a sample in a powder configuration rather than with a single crystal. Typical experimental data for both situations are given in figure 1 for comparison. A powder sample is composed of a large number of independent crystals (all of macroscopic size) exhibiting all possible orientations in space with the same probability. This sample is formally described by the assembly of $M$ identical crystals of volume $V_{\mathrm{tot}}/M$, containing $N/M$ unit cells. Note that the contribution of a powder of $M$ crystals of $N/M$ unit cells is equal to the contribution of only one single crystal of size $N$ averaged over all orientation in space. The integration is performed in reciprocal space on a sphere of radius $q_{hkl}$ as illustrated in figure 1 and the integrated powder intensity is

$$I_{\mathrm{powder}}^{\mathrm{int}}(q_{hkl}) = \frac{M}{V_{\mathrm{tot}}} \frac{N}{M} r_{\mathrm{e}}^2 \frac{1}{4\pi q_{hkl}^2} m_{hkl} |F_{hkl}|^2 \frac{(2\pi)^3}{V_{\mathrm{c}}}$$

$$= \frac{N}{V_{\mathrm{tot}}} r_e^2 \frac{2\pi^2}{q_{hkl}^2 V_{\mathrm{c}}} m_{hkl} |F_{hkl}|^2, \qquad (2.10)$$

where $m_{hkl}$ is the multiplicity of the $hkl$ Bragg reflection.

Again, the relevant quantity is $I_{\mathrm{powder}}^{\mathrm{int}}(q_{hkl})$, the integrated intensity of a Bragg peak on the radially averaged intensity $I_{\mathrm{powder}}(q)$. It may be useful to introduce peak-shaped function $L(q, q_{hkl})$ to model continuously $I_{\mathrm{powder}}(q)$ as follows:

$$I_{\mathrm{powder}}(q) = \frac{N}{V_{\mathrm{tot}}} r_{\mathrm{e}}^2 \frac{2\pi^2}{q^2 V_{\mathrm{c}}} \sum_{hkl} m_{hkl} |F_{hkl}|^2 L(q, q_{hkl}),$$
$$(2.11)$$

where the $L(q, q_{hkl})$ function is normalized as follows: $\int_q L(q, q_{hkl}) \mathrm{d}q = 1$.

For a powder sample, the two corrections are the $q^{-2}$ dependence of the intensity with respect to the scattering vector and the multiplicity term.

## 3. DIRECT AND INVERSE METHODS

In §2, we have shown how to deduce the values of the Fourier coefficients $F_{hkl}$ of the electron density $\rho(\boldsymbol{r})$ from experimental measurements of the Bragg peak

---

[2]For an oscillating single crystal (amplitude $\Delta\alpha$ along a rotation axis $Z'Z$), the integrated intensity measured for an individual Bragg peak $\boldsymbol{q}_{hkl}$ is divided by $\Delta\alpha|\boldsymbol{q}_{hkl}^{\mathrm{perp}}|$, where $|\boldsymbol{q}_{hkl}^{\mathrm{perp}}|$ is the component of $\boldsymbol{q}_{hkl}$ perpendicular to $Z'Z$. Note that Bragg peaks located along the rotation axis $Z'Z$ are not measured.

intensities. Once the $F_{hkl}$ values are known, there are two ways to obtain a structural model in real-space, the so-called direct and inverse methods. With the direct method approach, the structural model is built directly in real-space, and the Fourier coefficients $F_{hkl}$ are calculated from the model and compared with the experimental values. The different parameters of the model (size, contrast, disorder terms...) are adjusted by a least-squared minimization procedure to fit the experimental intensity. The main advantages of this method are: (i) to provide quantitative values of the parameters to describe the structural model, (ii) to be able to model the whole intensity curve (not only the Bragg peaks integrated intensities), and (iii) to introduce disorder terms in the description of the structure. The main drawbacks of a direct method are that a structural model has to be built already as a starting point, and that it may happen that several different models can fit as well the same experimental data. Inverse methods consist of the reconstruction of the electron density function, using an inverse Fourier transform from reciprocal space to real space. Its main advantage is to provide the global features of the structure without assuming initially any models. Dealing with periodic structures, the key point is to solve the 'phases problem', which may be complicated for a large number of Bragg peaks. As the reconstruction is based only on the integrated intensities of the Bragg peaks, it provides a periodic average structure but includes no disorder terms. The electron density maps are obtained with a finite spatial resolution, fixed by the accessible q-range and it is then more difficult to derive quantitatively the sizes of the structural units when compared with the direct methods. Before giving several examples of structure determination using both methods, we will describe the reconstruction of the electron density (§3.1) and the introduction of disorder contributions (§3.2).

### 3.1. Reconstruction of the electron density

The reconstruction of the electron density is obtained by an inverse Fourier transform from reciprocal space to the direct space, using the $F_{hkl}$ values (equation (2.9)):

$$\rho(\boldsymbol{r}) = \frac{1}{V_{\mathrm{c}}} \sum_{hkl} F_{hkl} \mathrm{e}^{+\mathrm{i}\boldsymbol{q}_{hkl}\cdot\boldsymbol{r}} = \frac{1}{V_{\mathrm{c}}} \sum_{hkl} F_{hkl} \mathrm{e}^{+\mathrm{i}2\pi(hx+ky+lz)}.$$

$$(3.1)$$

Experimentally, only $|F_{hkl}|^2$ is measured for $hkl$ values different from 000. The fact that only the modulus of a $F_{hkl}$ coefficient is measured is known at the 'phases problem' in crystallography and the $F_{hkl}$ coefficients are *a priori* complex numbers of unknown phase $\varphi_{hkl}$:

$$\rho(\boldsymbol{r}) = \frac{1}{V_{\mathrm{c}}} \sum_{hkl} F_{hkl} \mathrm{e}^{+\mathrm{i}\boldsymbol{q}_{hkl}\cdot\boldsymbol{r}}$$
$$= \frac{1}{V_{\mathrm{c}}} \sum_{hkl} |F_{hkl}| \mathrm{e}^{+\mathrm{i}\varphi_{hkl}} \mathrm{e}^{+\mathrm{i}2\pi(hx+ky+lz)}.$$

$$(3.2)$$

For the structures we are interested in, it happens that they all contain an inversion centre and the

space-group is centrosymmetric. If the origin of real space is taken at this inversion centre, the $F_{hkl}$ coefficients are real and a phase $\varphi_{hkl}$ can take only two discrete values, $\varphi_{hkl} = 0$ or $\pm\pi$:

$$\rho(\boldsymbol{r}) = \frac{F_{000}}{V_{\mathrm{c}}}$$
$$+ \frac{1}{V_{\mathrm{c}}} \sum_{hkl \neq 000} |F_{hkl}| \cos(\varphi_{hkl}) \cos(2\pi(hx+ky+lz)).$$

$$(3.3)$$

The 'phases problem' reduces to a sign determination ($\cos(\varphi_{hkl}) = \pm 1$) and it is very often possible to solve it. As the number of measured Bragg peaks is rather low, the usual method is to generate the electron density maps for all the different sign combinations. Among them, the best combination of signs is selected, which is in agreement with the independent knowledge of the structure in terms of the size of the building-blocks and the repartition of high and electron density regions. The complete sums of cosine terms for all space-groups are tabulated in the International Tables for Crystallography [1], more details are provided in[3] and an example of reconstruction for the $Ia\bar{3}d$ space group (electronic supplementary material, figure S2) is discussed in §6.

The $F_{000}$ coefficient cannot be measured because the scattering vector $\boldsymbol{q} = \boldsymbol{0}$ is not experimentally accessible. Consequently, as already mentioned (§2 equation (2.2)), only the relative variations of the electron density with respect to a constant electron density level can be determined. In practice, the value of the $F_{000}$ coefficient is obtained from the knowledge of the molecular composition of the sample. Either the average value $\langle\rho\rangle$ within the unit cell is taken, or the average variation $\langle\Delta\rho\rangle$ referring to a constant density level $\rho_0$ (for instance the solvent electron density for a colloidal suspension). In this latter case, the $F_{hkl}$ coefficients are relative to the Fourier transform of $\Delta\rho(\boldsymbol{r})$.

$$\rho(\boldsymbol{r}) = \langle\rho\rangle$$
$$+ \frac{1}{V_{\mathrm{c}}} \sum_{hkl \neq 000} |F_{hkl}| \cos(\varphi_{hkl}) \cos(2\pi(hx+ky+lz))$$

$$(3.4)$$

or

$$\rho(\boldsymbol{r}) = \rho_0 + \langle\Delta\rho\rangle + \frac{1}{V_{\mathrm{c}}} \sum_{hkl \neq 000}$$
$$|F_{hkl}| \cos(\varphi_{hkl}) \cos(2\pi(hx+ky+lz)).$$

In the case of a two-dimensional hexagonal phase, the lattice is two-dimensional and equation (5.3) has to be used instead.

---

[3]Note that the sum is performed over all the permutations and signs for each $hkl$ set (containing $m$ terms, where $m$ is the multiplicity) and that the $F_{hkl}$, $F_{khl}$, $F_{-hkl}$ ... are not always equal and may be related by an extra sign depending on the space group and its symmetry elements. For example, because of the sliding mirrors, $F_{khl} = (-1)^{h+k+l} F_{hkl}$ for the space group $Pm\bar{3}n$, and $F_{-hkl} = (-1)^{h+k} F_{hkl}$ and $F_{khl} = (-1)^{(h+k+l)/2} F_{hkl}$ for the space group $Ia\bar{3}d$.

### 3.2. Disorder contribution

It is possible to introduce some disorder contribution in a structural model based on direct methods. The nature of the disorder can be a displacement disorder over the lattice nodes (modelled by a Debye–Waller contribution), or a substitution disorder (distribution in size or in nature of some supra-molecular units). Another origin for disorder can be the conformation of the supra-molecular aggregates themselves, like for micelles of bloc-copolymers with long polymeric chains, that do not exhibit a spherical symmetry [11]. In this section, we will introduce only basic general equations, to show that all types of disorder affect scattering in the same way. When disorder is included, the unit cells are not identical, and a more general expression than in equation (2.6) applies, where one assumes that the structure is on average a three-dimensional periodic arrangement:

$$I(\boldsymbol{q}) = \frac{r_e^2}{V_{\text{tot}}} \left\langle \sum_{i=1}^{N} \sum_{j=1}^{N} F_i(\boldsymbol{q}) F_j^*(\boldsymbol{q}) \mathrm{e}^{-\mathrm{i}\boldsymbol{q}\cdot(\boldsymbol{R}_i - \boldsymbol{R}_j)} \right\rangle, \quad (3.5)$$

where $F_i(\boldsymbol{q}) = \int_{V_C} \rho_{(i)}(\boldsymbol{r}) \mathrm{e}^{-\mathrm{i}\boldsymbol{q}\cdot\boldsymbol{r}} \mathrm{d}\boldsymbol{r}$ refers to the content of the unit cell located at position $\boldsymbol{R}_i$. If one can assume that the disorder terms are not spatially correlated between two different unit cells, one can use the decoupling approximation that had been introduced in various contexts [10,12–14]

$$I(\boldsymbol{q}) \cong \frac{r_e^2}{V_{\text{tot}}} \sum_{i=1}^{N} \sum_{j=1}^{N} \langle F_i(\boldsymbol{q}) F_j^*(\boldsymbol{q}) \rangle \langle \mathrm{e}^{-\mathrm{i}\boldsymbol{q}\cdot(\boldsymbol{R}_i - \boldsymbol{R}_j)} \rangle \quad (3.6)$$

and the intensity reads:

$$I(\boldsymbol{q}) \cong \frac{r_e^2}{V_{\text{tot}}} N[|\langle F(\boldsymbol{q}) \rangle|^2 S(\boldsymbol{q}) + [\langle |F(\boldsymbol{q})|^2 \rangle - |\langle F(\boldsymbol{q}) \rangle|^2]]$$

$$= \frac{r_e^2}{V_{\text{tot}}} N \langle |F(\boldsymbol{q})|^2 \rangle [\beta(\boldsymbol{q}) S(\boldsymbol{q}) + 1 - \beta(\boldsymbol{q})]$$

with

$$\beta(\boldsymbol{q}) = \frac{|\langle F(\boldsymbol{q}) \rangle|^2}{\langle |F(\boldsymbol{q})|^2 \rangle}. \quad (3.7)$$

On this expression, one recovers the main important general result that the influence of disorder is twofold [10]. It gives rise to diffuse scattering in between the Bragg peaks (term $(1 - \beta(\boldsymbol{q}))$) and accordingly the intensities of the Bragg peaks are decreased by a factor $\beta(\boldsymbol{q})$.

In the case of a displacement disorder over the lattice nodes, the factor $\beta(\boldsymbol{q})$ is decreasing following an exponential law known as the Debye-Waller term:

$$\beta(\boldsymbol{q}) = \mathrm{e}^{-\langle u_{\boldsymbol{q}}^2 \rangle q^2}, \quad (3.8)$$

where $\langle u_{\boldsymbol{q}}^2 \rangle$ is the mean square amplitude of the displacement in the $\boldsymbol{q}$ vector direction. This expression can be simplified by assuming that the distribution is isotropic [10]. Then $\beta(\boldsymbol{q}) = \mathrm{e}^{-(q^2\langle u^2 \rangle/3)}$ for a three-dimensional lattice, and $\beta(\boldsymbol{q}) = \mathrm{e}^{-(q^2\langle u^2 \rangle/2)}$ for a two-dimensional lattice (like a two-dimensional hexagonal phase), where $\langle u^2 \rangle$ is the isotropic mean square amplitude of the displacement. Note that for bi-continuous cubic phases, expressions including the $\boldsymbol{q}$ vector direction dependence
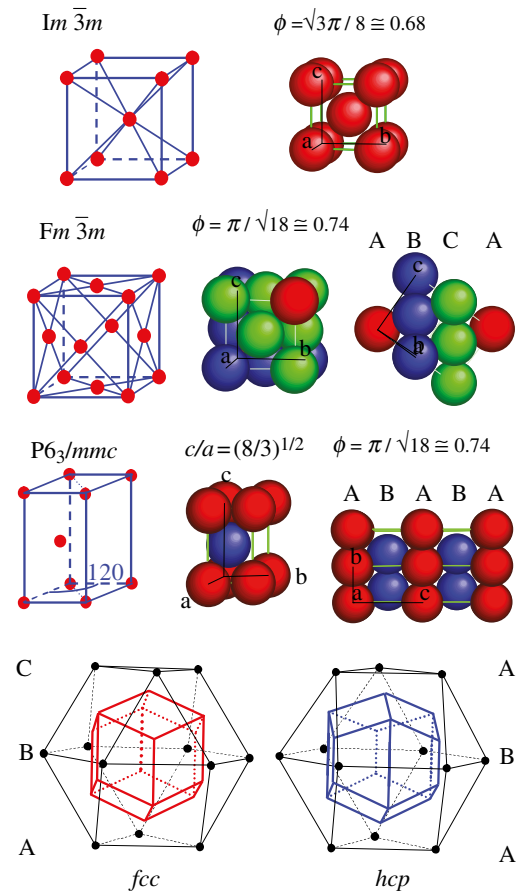
Figure 2. Three-dimensional packing of spheres: *bcc* (I$m\bar{3}m$), *fcc* (F$m\bar{3}m$) and *hcp* (P$6_3/mmc$). All sites are identical in these structures.

are available [15]. The values of $\langle u^2 \rangle$ have to be small and more precisely, by analogy with solid state theory, one can apply the Lindemann criterion for the melting of a solid, for which melting arises when $\langle u^2 \rangle / d \cong 0.1-0.2$, where $d$ is the typical interatomic distance [16]. For a mesophase, $d$ can be replaced by the typical distance between particles.

## 4. SPHERES PACKING AND *TCP* PACKING

Several mesophases consist of a three-dimensional packing of spherical-like particles. These particles display various natures such as LC dendrimers, micelles of surfactant molecules, micelles of block-copolymers and solid nanoparticles with organic chains grafted on their surface. The different, observed three-dimensional packings can be classified into two categories: spherical packing (*bcc*, *fcc* and *hcp*; figure 2 and table 1) and *tcp* (figure 3 and table 1). In the first category, all the particles are identical and have a spherical symmetry. In contrast, in a *tcp* packing, the particles are not all identical in the packing. They are located on lattice points with different symmetry ($Z = 12$, 14, 15, 16 nearest neighbours; figure 3) and are able to deform into spheroidal shapes because of their soft nature. Very often, one particular system can exhibit several of these packings upon concentration or temperature—for example, non-ionic surfactants in water [2,17,18] or dendrimers [3]. The global understanding of this behaviour is
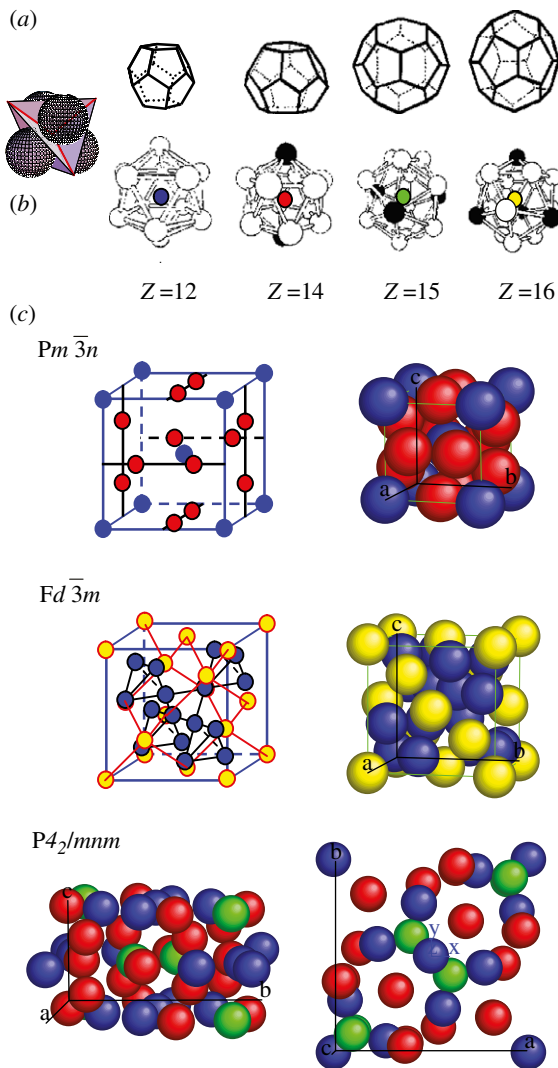
Figure 3. *Tcp* packing. (*a*) local tetrahedral close packing configuration. (*b*) the different sites $Z = 12$ (blue), $Z = 14$ (red), $Z = 15$ (green) and $Z = 16$ (yellow). (*c*) The three phases observed experimentally in soft matter systems: P$m\bar{3}n$, F$d\bar{3}m$ and P$4_2/mnm$.

based on the interaction potential between the particles and on the crystallization phenomena. The occurrence of *fcc* or *hcp* packing is related to the crystallization of spheres interacting via a hard-sphere potential and to the famous Kepler's conjecture in 1611. As recalled in figure 2, both structures consist of the dense packing of spheres with 12 nearest neighbours ($Z = 12$), and they have the same compacity of 0.74, but differ only in the packing sequence, ABC for *fcc* and AB for *hcp*. The Kepler's conjecture claims that both the *fcc* and *hcp* packings exhibit the largest possible compacity for the packing of identical spheres in three dimensions [19]. Surprisingly, a first proof of this conjecture has been given only very recently by the mathematician Thomas C. Hales, and is still nowadays under verification using extensive numerical calculations [20]. Recent numerical simulations using a hard-sphere potential find a very small entropy difference ($10^{-3}$ $k_B$ per sphere) in favour of the *fcc* packing versus the *hcp* one [21,22]. However, there are several observations of the *hcp* packing in soft matter systems [2,23,24] and in mesoporous materials [25], indicating that it could

also be thermodynamically stable. As the *bcc* packing exhibit a smaller compacity of 0.68 (instead 0.74 for *fcc/hcp*), its occurrence may at first sight be surprising. In fact, this packing occurs in the presence of a more long-range potential in addition to the hard-sphere potential [26–28]. A physical interpretation has been proposed by Kamien & Ziherl [29] in the case of dendrimers in terms of an additional repulsive potential driven by the conformational entropy of the chains located at the surface of the particles. This interpretation is, in fact, quite general and can be extended for many kind of particles where long enough chains are present on their surface. For example, for block-copolymer micelles with a shell made of EO chains, *fcc* packing is formed for short EO chains and *bcc* for longer ones [27].

For SAS, the *fcc*, *hcp* and *bcc* packings give rise to a simple expression for the $F_{hkl}$ coefficients (equation (2.9)), assuming that all particles are identical and have a spherical symmetry [14]:

$$F_{hkl} = \Delta\rho F_S(q_{hkl})f_{hkl}, \qquad (4.1)$$

where $F_S(q)$ is the form factor of a particle with a spherical symmetry and any density profile (sphere, core/shell . . . ) and $\Delta\rho$ is a contrast term. $f_{hkl} = \sum_n \mathrm{e}^{-i\boldsymbol{q}_{hkl} \cdot \boldsymbol{r}_n}$ is the structure factor inside the unit cell that depends on the lattice.[4] For sphere packing, both direct and inverse methods can be easily applied, and models with disorder terms are available [14]. In the case of *hcp*, a comparison of both methods confirmed the spherical shape of the micelles in this packing [23].

The *tcp* packings constitute a fascinating family of structures. In mesophases, thanks essentially to SAS experiments combined with reconstruction methods, three of them have been discovered so far (figure 3): the P$m\bar{3}n$, F$d\bar{3}m$ [30] and, more recently, the P$4_2/mnm$ phase [5,6,31]. Using purely geometrical arguments and the concept of geometrical frustration, Charvolin & Sadoc [32] have shown that *tcp* packings in mesophases are strongly related not only to the Franck and Kasper phases of metals and metallic alloys, but also to the structure of soap froths. It is remarkable that the P$m\bar{3}n$ phase has the same structure as one crystalline phase tungsten and the P$4_2/mnm$ phase as uranium [33]. In a geometrical approach, a *tcp* packing results from the compromise between a global constrain to achieve a periodic structure and a local minimum, the tetrahedral packing of four particles, which corresponds locally to a maximum density for spheres packing (figure 3). This compromise arises because it is not possible to form a periodic packing with regular tetrahedrons in three dimensions [34].

Then the particles are arranged locally in a tetrahedral configuration, but are not identical in the sense that they occupy sites with different symmetries, corresponding to different numbers of nearest neighbours ($Z = 12, 14, 15, 16 . . .$) (figure 3). The related geometrical problem with the domain of soap froths, which was brought up by Kelvin (1887), is to find the periodic soap froth with cells of identical volume that minimizes

---

[4]$f_{hkl} = 1 + (-1)^{h+k+l}$ for a *bcc* lattice, $f_{hkl} = 1 + (-1)^{h+k} + (-1)^{k+l} (-1)^{l+h}$ for a *fcc* lattice and $f_{hkl} = \mathrm{e}^{-2i\pi\frac{(h+2k)}{3}}\mathrm{e}^{-i\pi l/2} + \mathrm{e}^{-2i\pi\frac{(2h+k)}{3}} \mathrm{e}^{-3i\pi l/2}$ for an hcp lattice [2]. Values are given for example in Förster *et al.* [14].

the total area of the cells. Indeed, the minimization of the area corresponds locally to the Plateau's laws (1873) for soap films with a tetrahedral symmetry of the junctions of the films as depicted in figure 3. The minimization of this area is equivalent to the maximization of the density for spheres packing. Weaire & Phelan [35] have shown that the $P m\bar{3}n$ phase (with two types of cells) is a better solution to the Kelvin's problem than the packing of Kelvin's polyhedra [36]. For mesophases, Ziherl & Kamien [29,37] gave a physical interpretation of the minimisation of the total area in the $P m\bar{3}n$ phase by the maximization of the entropy of the chains located at the surface of the supra-molecular units. They were also able to compare the relative stability of the *bcc*, *fcc* and $P m\bar{3}n$ phases, using the combination of an hard-sphere potential with a repulsive soft shoulder potential [37].

In the case of soft deformable particles, their shape and size happen to modify slightly from a pure spherical symmetry depending on the site symmetry ($Z = 12, 14, 15, 16 \ldots$). In figure 3, the sites are depicted with different colours but spherical balls are used to simplify the representation. Inverse methods with SAS allow us to directly visualize differences in the shape and sizes depending on the symmetry of the site [3,30]. These methods are more suited to describe *tcp* packings than direct methods, which are in fact less used in this situation. This is because the form factor of each particle in the unit cell is different depending on its position, and cannot be factorized like in the case of spheres packing as shown in equation (4.1). For the $F d\bar{3}m$ structure, there is a significant difference in the size of the two types of sites ($Z = 12$ and $Z = 16$) that are both almost spherical [4,30]. In the $P m\bar{3}n$ structure (coexistence of $Z = 12$ and $Z = 14$), the $Z = 14$ sites adopt slightly elongated shapes as discussed in detail in Balagurusamy *et al.* [3]. In porous materials with a $P m\bar{3}n$ structure, the main cavities have two different sizes [38]. Moreover, additionnal pores may form between adjacent cavities and the whole structure can be described based on a new Infinite Periodic Minimal Surface (IPMS) by applying again a global criterium of aera minimization [39]. The $P 4_2/mnm$ structure contains 30 particles per unit cell ($Z = 12$, $Z = 14$ and $Z = 15$), and the reconstructions evidence spheroidal shapes for all of them, with small deformations from spherical symmetry [5,6]. Note that in the latter case, a characteristic feature is that the strongest Bragg reflections (table 1) have quite high Miller indices (*410, 330, 202, 212* ...) because of the large number (30) of particles in the unit cell. From the analogy with the Franck and Kasper phases, other *tcp* phases are still to be discovered in soft matter systems and mesoporous materials [40]. In this sense, there is also a structural link between *tcp* phases and the quasi-crystalline phases recently discovered in thermotropic dendrimers [5,33].

## 5. TWO-DIMENSIONAL HEXAGONAL PHASE

Two-dimensional hexagonal phases are very common in soft matter systems and nano-structured materials. For porous nano-structured materials, it has been shown that Bragg peaks intensity measurements with SAS are very useful to determine their pore size [41]. For this phase, the expressions of the intensity given in §2 have to be slightly modified because the lattice has two dimensions instead of three. In the following, using a simple model, we derive these expressions by assuming that the two-dimensional order is a true long-range order, and not a quasi-two-dimensional order like in the more sophisticated para-crystal model [14].

A two-dimensional hexagonal phase consists of the two-dimensional packing of very long particles having a cylindrical symmetry. A two-dimensional hexagonal lattice (electronic supplementary material, figure S1) and the macroscopic length $L$ along the perpendicular direction $z'z$ to the lattice describe this structure. The electron density $\rho(\boldsymbol{r})$ is a two-dimensional periodic function in the hexagonal plane and is constant along $z'z$. Equation (2.5), given previously in the three-dimensional case, changes in the following way:

$$
\begin{aligned}
|A(\boldsymbol{q})|^2 = L^2 \left( \frac{\sin\left((q_z L/2)\right)}{(q_z L/2)} \right)^2 F(\boldsymbol{q}_{\mathrm{P}})^2 \\
\times \mathsf{L}\left( \frac{\boldsymbol{q}_p \cdot \boldsymbol{a}}{2}, N_a \right) \mathsf{L}\left( \frac{\boldsymbol{q}_p \cdot \boldsymbol{b}}{2}, N_b \right),
\end{aligned} \tag{5.1}
$$

where $V_{\mathrm{C}} = S_{\mathrm{C}} L$ is the unit cell volume, $S_{\mathrm{C}}$ is the area of the two-dimensional unit cell defined by the basis vectors $(\boldsymbol{a}, \boldsymbol{b})$, $N = N_a N_b$ is the total number of two-dimensional unit cells and $\boldsymbol{r} = \boldsymbol{r}_{\mathrm{P}} + z\boldsymbol{e}_z$, $\boldsymbol{q} = \boldsymbol{q}_{\mathrm{P}} + q_z \boldsymbol{e}_z$,

$$
F(\boldsymbol{q}_P) = \int_{S_C} \rho(\boldsymbol{r}_p) e^{-\mathrm{i}\boldsymbol{q}\cdot\boldsymbol{r}_p} \mathrm{d}\boldsymbol{r}_p. \tag{5.2}
$$

Note that with this definition, $F(\boldsymbol{q}_{\mathrm{P}})$ has the dimension $[L^{-1}]$ but $\rho(\boldsymbol{r})$ is still defined as the three-dimensional electron density ($[L^{-3}]$). The expression for the electron density reconstruction then reads (see equation (3.4))

$$
\rho(\boldsymbol{r}) = \rho_0 + \langle \Delta\rho \rangle + \frac{1}{S_c} \sum_{hk \neq 00} F_{hk} e^{+\mathrm{i}2\pi(hx+ky)} \tag{5.3}
$$

with

$$
F_{hk} = \int_{S_C} \rho(\boldsymbol{r}_p) e^{-\mathrm{i}\boldsymbol{q}_{hk}\cdot\boldsymbol{r}_p} \mathrm{d}\boldsymbol{r}_p. \tag{5.4}
$$

The expressions for the intensity are derived essentially in the same way as in the three-dimensional case (equation (2.8); figure 1). The integrated intensity $I_{\mathrm{single}}^{\mathrm{int}}(\boldsymbol{q}_{hk})$ at a Bragg peak $\boldsymbol{q}_{hk} = 2\pi(h\boldsymbol{a}^* + k\boldsymbol{b}^*)$ is performed in a three-dimensional reciprocal volume $V_{hk}^*$ ($\boldsymbol{q} = q_a \boldsymbol{a}^* + q_b \boldsymbol{b}^* + q_z \boldsymbol{e}_z$). As the length $L$ is large, the extension of a Bragg peak along $z'z$ is small. The integration gives

$$
\begin{aligned}
I_{\mathrm{single}}^{\mathrm{int}}(\boldsymbol{q}_{hk}) &= \frac{r_{\mathrm{e}}^2}{V_{\mathrm{tot}}} \int_{V_{hk}^*} |A(\boldsymbol{q}_{hk} + \boldsymbol{q})|^2 \mathrm{d}\boldsymbol{q} \\
&= \frac{N}{V_{\mathrm{tot}}} r_{\mathrm{e}}^2 |F_{hk}|^2 (2\boldsymbol{\pi})^3 \frac{L}{S_c}.
\end{aligned} \tag{5.5}
$$

For a powder sample, equations (2.10) and (2.11)) becomes

$$I_{powder}^{int}(q_{hk}) = \frac{N}{V_{tot}} r_e^2 \frac{2\pi^2}{q_{hk}^2} m_{hk} |F_{hk}|^2 \frac{L}{S_c} \qquad (5.6)$$

and

$$I_{powder}(q) = \frac{N}{V_{tot}} r_e^2 \frac{2\pi^2}{q^2} \frac{L}{S_c} \sum_{hk} m_{hk} |F_{hk}|^2 L(q, q_{hk}), \quad (5.7)$$

where $m_{hk}$ is the multiplicity of the $hk$ Bragg reflection.

Like in the three-dimensional case, a $q^{-2}$ dependence applies for a powder sample. This behaviour can be derived in a slightly different way [14,42–44] as the product of a $q^{-1}$ contribution in the hexagonal plane (orientation average of the two-dimensional lattice) and a $q^{-1}$ dependence of a form factor along $z'z$. Assuming that the particles packed on the two-dimensional lattice have a cylindrical symmetry, one can introduce their cross section form factor $F_{CS}(q)$, in a similar way as for sphere packing (equation (4.1)):

$$F(\boldsymbol{q}_P) = \Delta\rho \int_{disk} e^{-i\boldsymbol{q}_p \cdot \boldsymbol{r}_p} d\boldsymbol{r}_p = \Delta\rho(\pi R^2)\frac{2J_1(qR)}{qR} = \Delta\rho F_{CS}(q)$$

and

$$I_{powder}(q) = \frac{N}{V_{tot}} r_e^2 \frac{2\pi^2}{q^2} \frac{L}{S_c} \Delta\rho^2 |F_{CS}(q)|^2 \sum_{hk} m_{hk} L(q, q_{hk}).$$
$$(5.8)$$

Similar to spheres packing, both direct and inverse methods are available for two-dimensional hexagonal phases. Contribution of disorder [14,42,43] can also be included as introduced in §3.2. In figure 4, a comparison of both methods is given in the case of the formation of a two-dimensional hexagonal hybrid material (SBA-15). On the basis of the Bragg peaks evolution upon time (figure 4a), the variations of the electron density are modelled either by a core/shell form factor [43,45] or by performing a two-dimensional electron density reconstruction [46]. The time-resolved formation of a dense silica wall in-between the cylindrical micelles is evidenced with both methods.

# 6. BI-CONTINUOUS AND TRI-CONTINUOUS PHASES

In bi-continuous (figure 5) and tri-continuous cubic (figure 6) phases, the structural units are not individual particles (such as spheres or cylindrical particles) but continuous three-dimensional periodic interfaces and their description require the use of the crystallography of surfaces [34]. To our knowledge, only three different bi-continuous phases has been observed. Their space-groups are (Ia$\bar{3}$d, Pn$\bar{3}$m, Im$\bar{3}$m; table 1), corresponding respectively to the three Infinite Periodic Minimal Surfaces (IPMS) G, D and P surfaces. Only one tri-continuous phase [8] of space-group Im$\bar{3}$m has been discovered. We can underline here again that the knowledge of the space-group is not sufficient for the structure identification, as the space-group Im$\bar{3}$m corresponds to three different mesophases (table 1): *bcc* sphere packing,
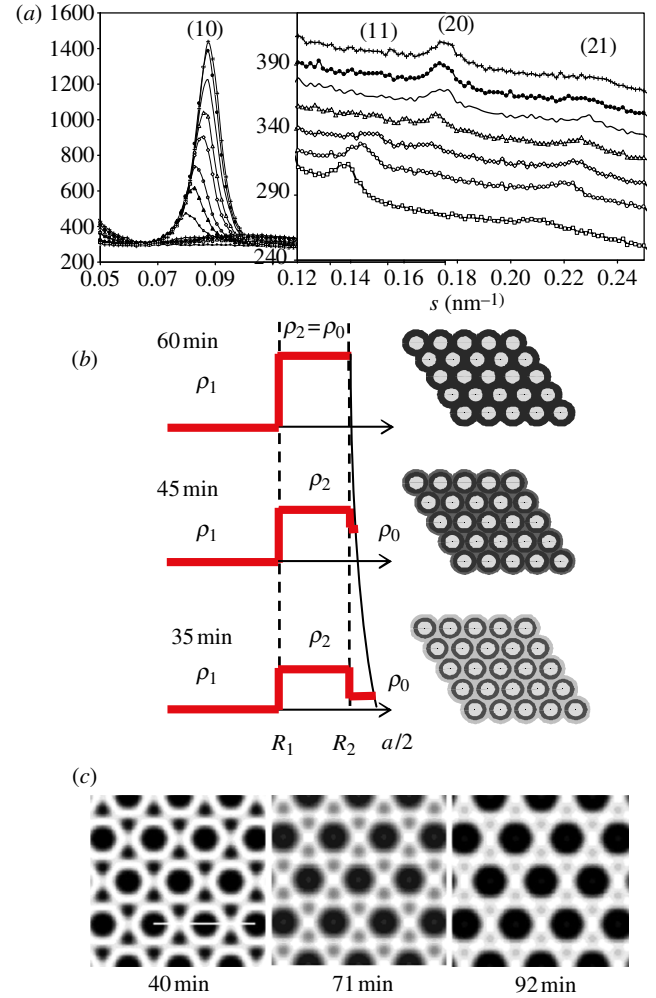


Figure 4. Time-resolved formation of a two-dimensional hexagonal nano-structured silica material (SBA-15). (a) Evolution of the (10), (11), (20) and (21) Bragg peaks (powder pattern). (b) Density profile obtained by modeling these experimental data using a cylindrical core/shell model (higher electron density in black) [45]. (c) Two-dimensional electron density reconstruction (higher electron density in white) from reference [46]. The formation upon time of a dense silica wall in-between the cylindrical micelles is evidenced with both methods.

P-surface bi-continuous cubic phase and the tri-continuous cubic phase. In the latter case, a characteristic feature is that the strongest Bragg reflections are the *321* and *400*, indicating that many different structural units are present in the unit cell.

## 6.1. Bi-continuous Ia$\bar{3}$d

Since the pioneer work by Luzzati & Spegt [7] who discovered this type of structure in the case of the Ia$\bar{3}$d space-group about 40 years ago, inverse as well as direct methods have been developed based on the use of the Bragg peaks intensities. We will focus here only on this space-group although similar expressions for SAS can be derived for the two others bi-continuous phases (D and P surfaces).

The main feature in the case of the Ia$\bar{3}$d space-group is that it gives rise to two strong Bragg reflections, the *211* and the *220* (figure 1 and table 1). Performing an electron density reconstruction based only on the two terms $F_{211}$

rods model                                                    G-surface model
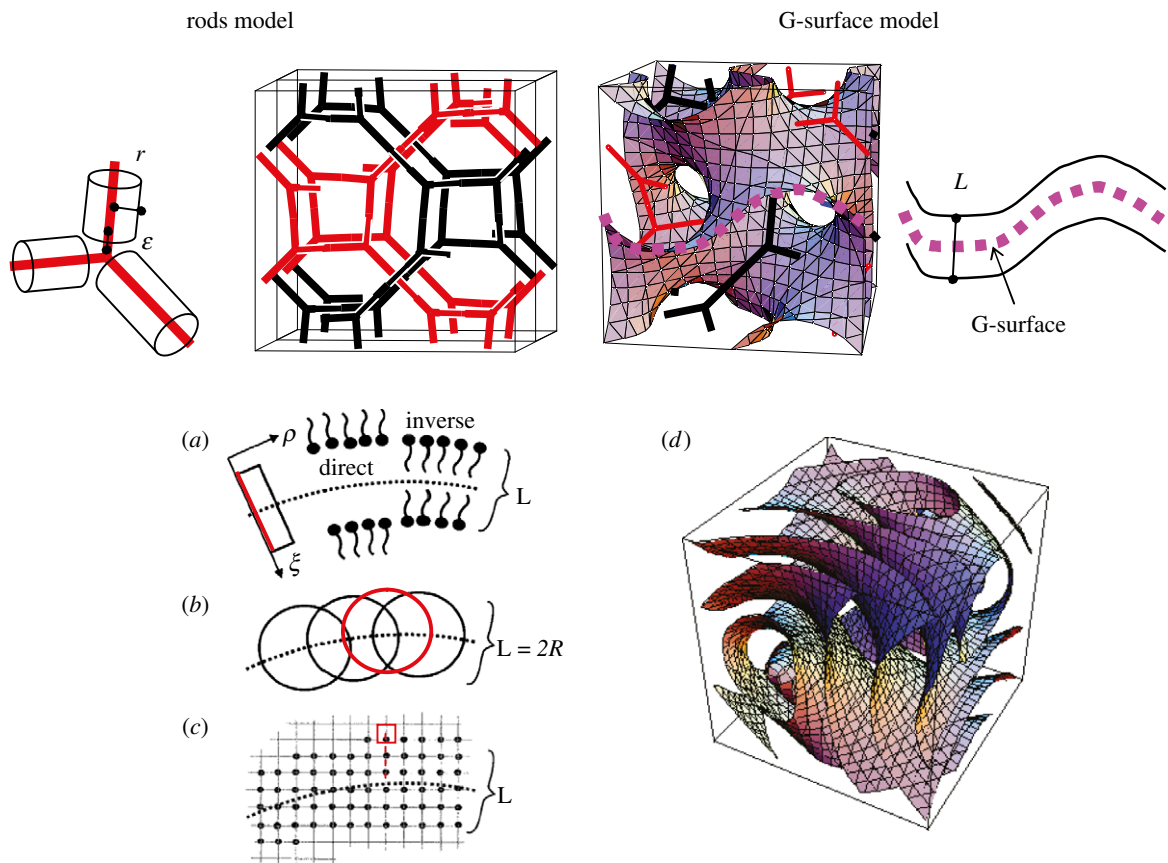


Figure 5. The cubic unit cell for the $I a \bar{3} d$ bi-continuous phase for the rods model and the G-surface model. Using the G-surface model, different methods can be used [14] to take into account the thickness of the film $L$ (*a*) a linear profile along the normal at each point of the surface [47] (*b*) a convolution by an infinitely thin shell [48] (*c*) a lattice method with the calculation of the distance to the G-surface [49] (*d*) the iso-density surfaces using the nodal surfaces approximation [50].

and $F_{220}$ reproduces well the bi-continuous structure, as shown in electronic supplementary material, figure S2. This is a good illustration of the efficiency of inverse methods to elucidate new structures. Further refinement of the structure can be done by including the other measured Bragg reflections. To solve the phase problem, comparison with electron microscopy images were used for both lipids phases [30] and mesoporous materials [51,52].

The alternative way is to model completely the Bragg intensities using the structure factor of the G-surface. Another possibilty is to calculate the structure factor of the two networks (rods model in figure 5), adding a cylindrical molecular form factor on each rod [7], but this method is less satisfying because it involves one more adjustable parameter, $\varepsilon$, a cut-off on the rods length (figure 5). Using the G-surface model, the structure is described essentially by a film of thickness $L$ and an electron density $\rho_1$, which is centred on the G-surface and separates the two subspaces of density $\rho_0$ with an associated contrast $\Delta\rho = |\rho_1 - \rho_0|$. Starting from equation (2.9), we get

$$F_{hkl} = \int_{V_C} \rho(\boldsymbol{r}) \mathrm{e}^{-\mathrm{i}\boldsymbol{q}_{hkl}\cdot\boldsymbol{r}} \mathrm{d}\boldsymbol{r} = \int_{V_{\mathrm{film}}} \Delta\rho \mathrm{e}^{-\mathrm{i}\boldsymbol{q}_{hkl}\cdot\boldsymbol{r}} \mathrm{d}\boldsymbol{r} \quad (6.1)$$

and, in the limit of an infinitely thin film:

$$F_{hkl} = \Delta\rho L \int_{A_G} \mathrm{e}^{-2\mathrm{i}\pi(hx+ky+lz)} \mathrm{d}S = \Delta\rho L a^2 f_{hkl}^G \quad (6.2)$$

with

$$f_{hkl}^G = \frac{1}{a^2} \int_{A_G} \mathrm{e}^{-2\mathrm{i}\pi(hx+ky+lz)} \mathrm{d}S. \quad (6.3)$$

The $f_{hkl}^G$ coefficients are the structure factors of the G-surface and $A_G = 3.091 a^2$ is the area of the G-surface in the cubic unit cell. We calculated the G-surface structure factors $f_{hkl}^G$ using the exact G-surface IPMS [48] and their values are given in electronic supplementary material, table S1 along with more recent calculations [15,47]. Using the approximation of the G-surface by Von Schnering & Nesper [53] by a nodal surface of equation

$$\sin(2\pi x)\cos(2\pi y) + \sin(2\pi y)\cos(2\pi z)$$
$$+ \sin(2\pi z)\cos(2\pi x) = 0, \quad (6.4)$$

the calculation of the structure factors is much simplified, and the values (electronic supplementary material, table S1) are close enough to those of the G-surface to be used instead.

To take into account the thickness of the film, $L$, we introduced a simple method where the points on the G-surface are convoluted in real space by an infinitely thin spherical shell of radius $R=L/2$ (figure 5) [48]. The main advantage of this method is that the form factor of this spherical shell ($4\pi R^2(\sin(qR)/qR)$) appears simply as a product in the expression of $F_{hkl}$
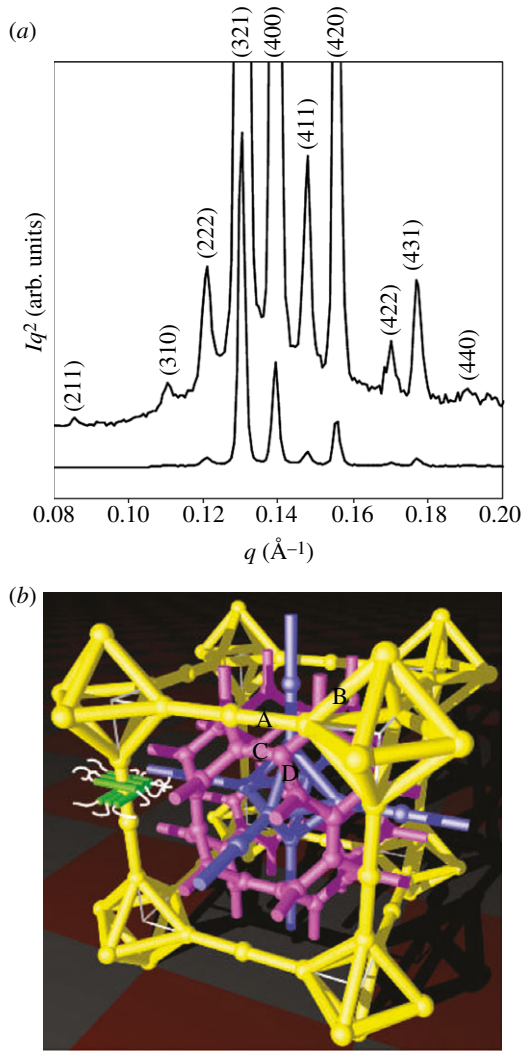
Figure 6. The $I m\bar{3} m$ tri-continuous cubic phase [8]. (*a*) Powder pattern. (*b*) Network model derived from the electron density reconstruction. The two identical networks are drawn in yellow and violet and the third one in magenta.

because of the spherical symmetry of the shell:

$$F_{hkl} = n_{\rm S} \rho_{\rm S} \int_{\rm shell} e^{-i\boldsymbol{q}_{hkl}\cdot\boldsymbol{r}} {\rm d}\boldsymbol{r} \int_{A_{\rm G}} e^{-2i\pi(hx+ky+lz)} {\rm d}S$$

$$= n_{\rm S} \rho_{\rm S} 4\pi R^2 \frac{\sin(q_{hkl}R)}{q_{hkl}R} a^2 f_{hkl}^G, \qquad (6.5)$$

where $n_{\rm S}$ is the two-dimensional number density of the shells on the G-surface, and $\rho_{\rm S}$ the two-dimensional electron density on a shell. The product $n_{\rm S} \cdot \rho_{\rm S}$ is related to the contrast $\Delta\rho$ of the film ( $n_{\rm S} A_{\rm G} \rho_{\rm S} 4\pi R^2 = \Delta\rho V_{\rm film}$ ) and $V_{\rm film}$ can be calculated using the Gauss–Bonnet relation ( $V_{\rm film} = 2RA_{\rm G} - (32\pi/3)R^3$ ) [48]. Taking into account the thickness $L = 2R$, the final expression reads

$$F_{hkl} = \Delta\rho \frac{V_{\rm film}}{A_{\rm G}} \frac{\sin(q_{hkl}R)}{q_{hkl}R} a^2 f_{hkl}^G$$

$$= \Delta\rho 2R \left(1 - \frac{16\pi}{3} \frac{R^2}{3.091 a^2}\right) \frac{\sin(q_{hkl}R)}{q_{hkl}R} a^2 f_{hkl}^G. \quad (6.6)$$

This model is valid only for sufficiently small values of $R$ with respect to the mean curvature radius of the G-surface, typically for an $R/a$ ratio less than 0.25 [48]. In the

intensity expression, a disorder term can be introduced using the Debye–Waller expression (refer to §3.2). More refined models are available in the literature, but without a simple factorization of a spherical form factor. Garstecki & Holyst [15,54–57], Harper *et al.* [47], Enlow *et al.* [49] took into account the thickness either by a segment of length $L$ oriented at each point along the normal to the G-surface, or using a lattice model (figure 5). Using parallel nodal surfaces (see equation (6.4) and figure 5), Solovyov *et al.* [50] obtained a very precise modelization of a meso-porous $I a\bar{3} d$ phase based on more than 25 Bragg reflections. It is found that the thickness of the silica region is almost constant and homogenous, with a slightly higher density (10%) at the flat points of the G-surface.

## 6.2. Tri-continuous $I m\bar{3} m$

Until now, the tri-continuous $I m\bar{3} m$ phase has been observed only with thermotropic compounds [8,9,58]. However, we believe that mesophase formation again probably results from the segregation between two molecular entities (aliphatic chains and polar cores for these thermotropic compounds) like for the previously mentioned structures. One then expects that new examples of this phase will be discovered in other systems such as lyotropic systems or nano-structured materials. For such complicated topology, the use of a reconstruction method was necessary to elucidate its structure (figure 6) [8,59]. On the basis of the three main Bragg peaks (*321, 400* and *420*), the reconstruction evidences three interwoven regions in the structure, proving that it is tri-continuous. A network model has been proposed to visualize these three regions, as shown in figure 6. It consists of three networks. Only two of them are identical (drawn in yellow and violet in figure 6*b*), as the third one (drawn in magenta in figure 6*b*), located in between the two identical ones, is of a different type. A slightly different model that is also based on three networks has been recently proposed, and it is still in agreement with a tri-continuous structure [60]. For this phase, the challenges remaining are: (i) a visualization based on transmission electron microscopy studies to confirm the SAS results and (ii) a deeper understanding of its structural relationships with the $I a\bar{3} d$ bi-continuous phase. Indeed, a phase transition between these two cubic phases has been observed in several thermotropic systems [8,60].

## 7. CONCLUSION

This paper provides a summary of the available structural models for different three-dimensional meso-phases. Such complex structures all result from the packing of supra-molecular units having two incompatible molecular blocks and are encountered nowadays in various fields. For example, a recent application of these types of structures is to use them to obtain tunable optical properties, in synthetic nano-structured materials or in biological systems like butterflies wings [61]. Here, we focus on the use of SAS to establish structural models, and introduce two types of methods: the inverse and the direct ones. For sphere packing and two-dimensional hexagonal phases, structural models are easier to derive because there is a straightforward

factorization between a form factor and a structure factor in the SAS intensity expression. Then, more elaborated models including disorder terms may be even used for these phases. To investigate *tcp* packings, inverse methods are preferred because the particles in the unit cell have different form factors. For bi-continuous cubic phases, both methods are available in order to incorporate the film thickness but direct methods are better suited. We propose a simple model based on the convolution in the direct space of the IPMS by a spherical shell that leads to a factorization of its form factor in reciprocal space.

In the near future, two main developments are expected in the structural analysis of mesophases. The first is to include disorder terms of different kinds in the structural models. For example, there is a need to develop models for substitution disorder between different types of particles dealing with more and more elaborated multi-component nano-structured materials. A second challenge will be to introduce quantitatively the interaction potentials between soft deformable entities and to relate them to the mesophase structures, to ultimately predict the phase diagrams. One possible approach may be to measure these interaction potentials in concentrated solutions during mesophase formation using SAS.

# REFERENCES

1  1995 *International Tables for Crystallography.* Kluwer Academic Publishers.

2  Clerc, M. 1996 A new symmetry for the packing of amphiphilic direct micelles. *J. Phys.* **6**, 961–968. (doi:10.1051/jp2:1996110)

3  Balagurusamy, V. S. K., Ungar, G., Percec, V. & Johansson, G. 1997 Rational design of the first spherical supramolecular dendrimers self-organized in a novel thermotropic cubic liquid-crystalline phase and the determination of their shape by X-ray analysis. *J. Am. Chem. Soc.* **119**, 1539–1555. (doi:10.1021/ja963295i)

4  Delacroix, H., GulikKrzywicki, T. & Seddon, J. M. 1996 Freeze fracture electron microscopy of lyotropic lipid systems: quantitative analysis of the inverse micellar cubic phase of space group $F$d3m ($Q^{227}$). *J. Mol. Biol.* **258**, 88–103. (doi:10.1006/jmbi.1996.0236)

5  Ungar, G., Liu, Y. S., Zeng, X. B., Percec, V. & Cho, W. D. 2003 Giant supramolecular liquid crystal lattice. *Science,* **299**, 1208–1211. (doi:10.1126/science.1078849)

6  Bates, F. S., Lee, S. & Bluemle, M. J. 2010 Discovery of a Frank–Kasper σ phase in sphere-forming block copolymer melts. *Science* **330**, 349–353. (doi:10.1126/science.1195552)

7  Luzzati, V. & Spegt, P. A. 1967 Polymorphism of lipids. *Nature* **215**, 701–704. (doi:10.1038/215701a0)

8  Zeng, X. B., Ungar, G. & Imperor-Clerc, M. 2005 A triple-network tricontinuous cubic liquid crystal. *Nat. Mater.* **4**, 562–567. (doi:10.1038/nmat1413)

9  Levelut, A. M. & Clerc, M. 1998 Structural investigations on 'smectic D' and related mesophases. *Liquid Cryst.* **24**, 105–115. (doi:10.1080/026782998207631)

10  Guinier, A. 1994 *X-ray diffraction: in crystals, imperfect crystals, and amorphous bodies.* Dover publications.

11  Pedersen, J. S. 2001 Structure factors effects in small-angle scattering from block copolymer micelles and star polymers. *J. Chem. Phys.* **114**, 2839–2846. (doi:10.1063/1.1339221)

12  Kotlarchyk, M., Chen, S. H., Huang, J. S. & Kim, M. W. 1984 Structure of three-component microemulsions in the critical region determined by small angle neutron scattering. *Phys. Rev. A* **29**, 2054–2069. (doi:10.1103/PhysRevA.29.2054)

13  Pedersen, J. S. 1997 Analysis of small-angle scattering data from colloids and polymer solutions: modeling and least-squares fitting. *Adv. Colloid Interface* **70**, 171–210. (doi:10.1016/S0001-8686(97)00312-6)

14  Förster, S., Timmann, A., Konrad, M., Schellbach, C., Meyer, A., Funari, S. S., Mulvaney, P. & Knott, R. 2005 Scattering curves of ordered mesoscopic materials. *J. Phys. Chem. B* **109**, 1347–1360. (doi:10.1021/jp0467494)

15  Garstecki, P. & Holyst, R. 2002 Scattering patterns of self-assembled cubic phases. II. Analysis of the experimental spectra. *Langmuir* **18**, 2529–2537. (doi:10.1021/la011299h)

16  Arms, D. A., Shah, R. S. & Simmons, R. O. 2003 X-ray debye-waller factor measurements of solid $^3$He and $^4$He. *Phys. Rev. B* **67**, 094303. (doi:10.1103/PhysRevB.67.094303)

17  Sakya, P., Seddon, J. M., Templer, R. H.,, Mirkin, R. J. & Tiddy, G. J. T. 1997 Micellar cubic phases and their structural relationships: the nonionic surfactant system $C_{12}EO_{12}$/water. *Langmuir* **13**, 3706–3714. (doi:10.1021/la9701844)

18  Imai, M., Yoshida, I., Iwaki, T. & Nakaya, K. 2005 Static and dynamic structures of spherical nonionic surfactant micelles during the disorder-order transition. *J. Chem. Phys.* **122**, 044906. (doi:10.1063/1.1839559)

19  Hales, T. C. 2006 Sphere packing. IV. Detailed bounds. *Discrete Comput. Geom.* OF1–OF16. (doi:10.1007/s00454-005-1213-z)

20  Hales, T. C. 2005 A proof of the Kepler conjecture. *Ann. Math.* **162**, 1065–1185. (doi:10.4007/annals.2005.162.1065)

21  Mau, S. C. & Huse, D. A. 1999 Stacking entropy of hard-sphere crystals. *Phys. Rev. E* **59**, 4396–4401. (doi:10.1103/PhysRevE.59.4396)

22  Koch, H., Radin, C. & Sadun, L. 2005 Most stable structure for hard spheres. *Phys. Rev. E* **72**, 16708. (doi:10.1103/PhysRevE.72.016708)

23  Zeng, X. B., Liu, Y. S. & Imperor-Clerc, M. 2007 Hexagonal close packing of nonionic surfactant micelles in water. *J. Phys. Chem. B* **111**, 5174–5179. (doi:10.1021/jp0687955)

24  Shearman, G. C., Tyler, A. I. I., Brooks, N. J., Templer, R. H., Ces, O., Law, R.V. & Seddon, J. M. 2009 A 3-D hexagonal inverse micellar lyotropic phase. *J. Am. Chem. Soc.* **131**, 1678. (doi:10.1021/ja809280r)

25  Tolbert, S. H., Schaffer, T. E., Feng, J. L., Hansma, P. K. & Stucky, G. D. 1997 A new phase of oriented mesoporous silicate thin films. *Chem. Mater.* **9**, 1962–1967. (doi:10.1021/cm960454o)

26  Anderson, J. A., Lorenz, C. D. & Travesset, A. 2008 Micellar crystals in solution from molecular dynamics simulations. *J. Chem. Phys.* **128**, 184906. (doi:10.1063/1.2913522)

27  Hamley, I. W., Daniel, C., Mingvanish, W., Mai, S. M., Booth, C., Messe, L. & Ryan, A. J. 2000 From hard spheres to soft spheres: the effect of copolymer composition on the structure of micellar cubic phases formed by diblock copolymers in aqueous solution. *Langmuir* **16**, 2508–2514. (doi:10.1021/la991035j)

28  McConnell, G. A. & Gast, A. P. 1996 Predicting disorder–order phase transition in polymeric micelles. *Phys. Rev. E* **54**, 5447–5455. (doi:10.1103/PhysRevE.54.5447)

29  Kamien, R. D. & Ziherl, P. 2001 Maximizing entropy by minimizing area: towards a new principle of

self-organization. *J. Phys. Chem. B* **105**, 10 147–10 158. (doi:10.1021/jp010944q)

30 Mariani, P., Luzzati, V. & Delacroix, H. 1988 Cubic phases of lipid—containing systems: structure analysis and biological implications. *J. Mol. Biol.* **204**, 165–189. (doi:10.1016/0022-2836(88)90607-9)

31 Garcia-Bennett, A. E., Kupferschmidt, N., Sakamoto, Y., Che, S. & Terasaki, O. 2005 Synthesis of mesocage structures by kinetic control of self-assembly in anionic surfactants. *Angew. Chem., Int. Ed.* **44**, 5317–5322. (doi:10.1002/anie.200500113)

32 Charvolin, J. & Sadoc, J. F. 1988 Periodic systems of frustrated fluid films and « micellar » cubic structures in liquid crystals. *J. Phys. France* **49**, 521–526. (doi:10.1051/jphys:01988004903052100)

33 Ungar, G. & Zeng, X. B. 2005 Frank–Kasper, quasicrystalline and related phases in liquid crystals. *Soft Matter* **1**, 95–106. (doi:10.1039/b502443a)

34 Sadoc, J. F. 1990 *Geometry in condensed matter physics.* World Scientific Publishing.

35 Weaire, D. & Phelan, R. 1994 A counterexample to Kelvin's conjecture on minimal surfaces. *Phil. Mag. Lett.* **69**, 107–110. (doi:10.1080/09500839408241577)

36 Rivier, N. 1994 Kelvin's conjecture on minimal froths and the counter-example of Weaire and Phelan. *Phil. Mag. Lett.* **69**, 297–303. (doi:10.1080/09500839408241607)

37 Kamien, R. D., Kung, W. & Ziherl, P. 2004 The foam analogy: from phases to elasticity. *J. Colloid Interface Sci.* **275**, 539–547. (doi:10.1016/j.jcis.2004.03.009)

38 Sakamoto, Y., Kaneda, M., Terasaki, O., Zhao, D. Y., Kim, J. M., Stucky, G., Shim, H. J. & Ryoo, R. 2000 Direct imaging of the pores and cages of three-dimensional mesoporous materials. *Nature* **408**, 449–453. (doi:10.1038/35044040)

39 Anderson, M. W., Egger, C. C., Tiddy, G. J. T., Casci, J. L. & Brakke, K. A. 2005 A new minimal surface and the structure of mesoporous silicas. *Angew. Chem. Int. Ed.* **44**, 3243–3248. (doi:10.1002/anie.200462295)

40 Sakamoto, Y. & Terasaki, O. 2011 A layer stacking with large repeating unit in multi-modal cage-type anionic-surfactant-templated silica mesoporous crystal. *Solid State Sci.* **13**, 762–767. (doi:10.1016/j.solidstatesciences.2010.04.006)

41 Imperor-Clerc, M., Davidson, P. & Davidson, A. 2000 Existence of a microporous corona around the mesopores of silica-based sba-15 materials templated by triblock copolymers. *J. Am. Chem. Soc.* **122**, 11 925–11 933. (doi:10.1021/ja002245h)

42 Palmqvist, A. E. C., Sundblom, A., Oliveira, C. L. P. & Pedersen, J. S. 2009 Modeling in situ small-angle X-ray scattering measurements following the formation of mesostructured silica. *J. Phys. Chem. C* **113**, 7706–7713. (doi:10.1021/jp809798c)

43 Manet, S. *et al.* 2011 Kinetics of the formation of a 2D-hexagonal silica nano-structured materials by non-ionic copolymer templating in solution. *J. Phys. Chem. B* **115**, 11 330–11 344. (doi:10.1021/jp200213k)

44 Glatter, O. & Freiberger, N. 2006 Small-angle scattering from hexagonal liquid crystals. *J. Phys. Chem. B* **110**, 14 719–14 727. (doi:10.1021/jp0559332)

45 Khodakov, A. Y., Zholobenko, V. L., Imperor-Clerc, M. & Durand, D. 2005 Characterization of the initial stages of SBA-15 synthesis by *in situ* time-resolved small-angle X-ray scattering. *J. Phys. Chem. B* **109**, 22 780–22 790. (doi:10.1021/jp052786z)

46 Linden, M., Flodstrom, K., Teixeira, C. V., Amenitsch, H. & Alfredsson, V. 2004 In situ synchrotron small-angle x-ray

scattering/x-ray diffraction study of the formation of SBA-15 mesoporous silica. *Langmuir* **20**, 4885–4891. (doi:10.1021/la049637c)

47 Harper, P. E., Gruner, S. M., Lewis, R. N. A. H. & McElhaney, R. N. 2000 Electron density modeling and reconstruction of infinite periodic minimal surfaces (IPMS) based phases in lipid-water systems. II. Reconstruction of D surface based phases. *Eur. Phys. J. E* **2**, 229–245. (doi:10.1007/PL00013664)

48 Clerc, M. & Duboisviolette, E. 1994 X-ray scattering by bicontinuous cubic phases. *J. Phys.* **4**, 275–286. (doi:10.1051/jp2:1994128)

49 Enlow, J. D., Enlow, R. L., McGrath, K. M. & Tate, M. W. 2004 Modeling liquid crystal bilayer structures with minimal surfaces. *J. Chem. Phys.* **120**, 1981–1989. (doi:10.1063/1.1635811)

50 Solovyov, L. A., Belousov, O. V., Dinnebier, R. E., Shmakov, A. N. & Kirik, S. D. 2005 X-ray diffraction structure analysis of MCM-48 mesoporous silica. *J. Phys. Chem. B* **109**, 3233–3237. (doi:10.1021/jp0482868)

51 Sakamoto, Y., Kim, T. W., Ryoo, R. & Terasaki, O. 2004 Three-dimensional structure of large-pore mesoporous cubic $Ia\bar{3}d$ silica with complementary pores and its carbon replica by electron crystallography. *Angew. Chem. Int. Ed.* **43**, 5231–5234. (doi:10.1002/anie.200460449)

52 Zhao, D. Y. *et al.* 2004 Facile synthesis and characterization of novel mesoporous and mesorelief oxides with gyroidal structures. *J. Am. Chem. Soc.* **126**, 865–875. (doi:10.1021/ja037877t)

53 Vonschnering, H. G. & Nesper, R., 1991 Nodal surfaces of fourier series: fundamental invariants of structured matter. *Z. Phys. B, Condens. Matter* **83**, 407–412. (doi:10.1007/BF01313411)

54 Garstecki, P. & Holyst, R. 2000 Surfaces, interfaces, and materials—scattering on triply periodic minimal surfaces—the effect of the topology, Debye–Waller, and molecular form factors. *J. Chem. Phys.* **113**, 3772–3779. (doi:10.1063/1.1287426)

55 Garstecki, P. & Holyst, R. 2001 Periodic surfaces of simple and complex topology: comparison of scattering patterns. *Phys. Rev. E* **64**, 021501.

56 Garstecki, P. & Holyst, R. 2001 Scattering patterns of self-assembled gyroid cubic phases in amphiphilic systems. *J. Chem. Phys.* **115**, 1095–1099. (doi:10.1063/1.1379326)

57 Garstecki, P. & Holyst, R. 2003 Scattering patterns of multiply continuous cubic phases in block copolymers. I. The model. *Macromolecules* **36**, 9181–9190. (doi:10.1021/ma0212588)

58 Imperor-Clerc, M. 2005 Thermotropic cubic mesophases. *Curr. Opin. Colloid Interface Sci.* **9**, 370–376. (doi:10.1016/j.cocis.2004.12.004)

59 Ungar, G., Zeng, X. B., Cseh, L. L. & Mehl, G. H. 2008 Testing the triple network structure of the cubic $Im\bar{3}m$ (I) phase by isomorphous replacement and model refinement. *J. Mater. Chem.* **18**, 2953–2961. (doi:10.1039/b805965a)

60 Kutsumizu, S., Mori, H., Saito, K., Yarnamoto, K., Sakurai, S. & Sakajiri, K. 2010 Temperature-jump time-resolved X-ray diffraction study of cubic-cubic phase-transition kinetics in thermotropic cubic mesogen 1,2-Bis(4'-n-alkoxybenzoyl)hydrazines (BABH-n). *Langmuir* **26**, 11 605–11 608. (doi:10.1021/la101553j)

61 Saranathan, V., Osuji, C. O., Mochrie, S. G. J., Noh, H., Narayanan, S., Sandy, A., Dufresne, E. R. & Prum, R. O. 2010 Structure, function, and self-assembly of single network gyroid (I4₁32) photonic crystals in butterfly wing scales. *Proc. Natl Acad. Sci. USA* **107**, 11 676–11 681. (doi:10.1073/pnas.0909616107)